Faulty Phase Localization and Severity Estimation of Interturn Short-Circuit Fault in PMSG of Wind Power System Under Wind Fluctuations

Bin Sun, Ying Zhu, *Member, IEEE*, and Zhinong Wei, *Member, IEEE*

***Abstract*—Interturn short-circuit fault (ISCF) is among the most common electrical faults in permanent magnet synchronous generators (PMSGs), with subtle early indicators that make detection challenging, especially under wind fluctuations. To improve the reliability of wind power systems and extend the lifespan of PMSGs, this article presents an innovative approach for localizing faulty phase and estimating the severity of ISCF. First, the root mean square (RMS) of stator current space vector (SCSV) is measured as the diagnostic variable. Subsequently, a novel one-dimensional convolutional neural networks digital twin model is developed, accounting for wind fluctuations to calculate the reference RMS of SCSV. Fault diagnosis is conducted by analyzing the residuals between the measured values and the reference values, complemented by adaptive thresholds, which innovatively adjusts based on wind variation rate. Finally, the faulty phase is localized through the phase current, and the severity is estimated by comparing the measured SCSV RMS with the calculated value. Experiments on a specially designed motor drive platform yielded 2 million health data samples under different wind conditions for model training. The proposed method demonstrated high sensitivity and robustness, even for the minor faults, outperforming various existing approaches.**

***Index Terms*—Adaptive threshold, current space vector, digital twin model, interturn short-circuit fault, one-dimensional convolutional neural networks (1D-CNNs), permanent magnet synchronous generator (PMSG), wind fluctuations.**

I. Introduction

WIND energy, recognized as a critical renewable energy source to replace fossil fuel-based power generation that contributes to environmental pollution and climate change, has witnessed substantial global development [1], [2], [3]. Among wind power technologies, permanent magnet synchronous generator (PMSG) wind power systems have emerged as an important solution, particularly in offshore applications at megawatt-scale power ratings. This predominance stems from their distinctive technical features including gearless direct-drive configuration, elimination of separate excitation systems, and superior grid fault ride-through performance [4], [5], [6], [7].

PMSGs operating in offshore wind farms are subjected to harsh environmental conditions, including high salinity and humidity, making fault tolerance a critical performance indicator. Electrical faults in PMSGs can lead to partial loss of functionality or even complete system failure, underscoring the importance of fault diagnosis for the safe operation of wind power systems [8], [9].

To maximize power generation efficiency, generators in wind power systems must operate continuously for extended periods. Thus, PMSGs are susceptible to various faults, such as interturn short-circuit fault (ISCF), open circuit fault, and demagnetization fault [10], [11], [12], [13], with ISCF being the most prevalent [14]. ISCF can induces significant circulating current within the short-circuit loop. If not promptly detected and rectified, ISCF can escalates into more severe issue, such as phase-to-phase short-circuit or ground fault, potentially resulting in the shutdown of the wind power system [15].

Currently, numerous scholars have conducted research on faults in PMSGs. Typical ISCF diagnosis methods are based on analytical models [16], [17], [18], [19], [20], signal analysis [21], [22], [23], [24], [25], and data-driven approaches [26], [27], [28], [29], [30], [31].

Model-based methods identify the fault type and location by developing an ISCF model that incorporates the motor's electrical parameters. For instance, a method based on dynamic response model is developed for detecting ISCF in permanent magnet synchronous motors (PMSMs) [17]. In this method, the fault is detected by compensating for harmonic spikes caused by speed and torque changes. In [18], an adaptive detection method based on the bandwidth variations of dual-loop controllers is proposed to enhance the robustness and accuracy of ISCF detection in PMSGs. Qin et al. [19] proposed an analytical fault model based on pulsewidth modulation (PWM) voltages for the diagnosis of an ISCF in PMSM, utilizing PWM harmonics to characterize fault currents. These model-based approaches enable real-time fault detection when precise parameters are utilized. However, acquiring precise model parameters remains a challenge due to the inherent nonlinearity of motor dynamics and the variability of machine parameters under different operating conditions.

The signal analysis methods focus on analyzing selected signals to extract fault characteristics, utilizing approaches such

Received 20 January 2025; revised 24 March 2025; accepted 2 April 2025. Date of publication 9 April 2025; date of current version 30 June 2025. This work was supported by the National Natural Science Foundation of China under Grant 52477045. Recommended for publication by Associate Editor M. S. ElMoursi. *(Corresponding author: Ying Zhu.)*

The authors are with the School of Electrical and Power Engineering, Hohai University, Nanjing 211100, China (e-mail: binsun@hhu.edu.cn; yingzhu@hhu.edu.cn; znwei@hhu.edu.cn).

Color versions of one or more figures in this article are available at https://doi.org/10.1109/TPEL.2025.3559297.

Digital Object Identifier 10.1109/TPEL.2025.3559297

as signal injection, vibration signals, and current signals. Among these, current feature-based analysis is the most prevalent, with researchers like Rosero et al. [23] employing empirical mode decomposition combined with Wigner-Ville distribution for diagnosing ISCF fault through stator current analysis. In [24], an online ISCF diagnosis method based on current trajectory analysis is proposed, utilizing the phase currents output by the motor controller to eliminate the need for additional hardware circuits. In addition, Chen et al. [25] detected ISCF in SRM by analyzing the asymmetry of phase currents and using the ratio of negative to positive sequence components as a fault index. This signal-based method has significant advantages in terms of real-time performance and efficiency, but it faces challenges in feature extraction and dependence on signal quality.

In recent years, with the advancement of computer technology, data-driven approaches have rapidly evolved. This approach leverages artificial intelligence techniques to achieve fault diagnosis through machine learning, reasoning, and decision-making methods. Wei et al. [26] designed a residual convolutional deep learning model targeting ISCF fault, demonstrating robust performance under variations in bandwidth for speed and current controllers. Li et al. [27] proposed a fault diagnosis method based on conditional generative adversarial networks, which enhanced diagnostic accuracy in scenarios with insufficient labeled data. Wu et al. [28] established an unsupervised learning method for ISCF diagnosis by extracting inherent data patterns from unlabeled samples. Chen et al. [29] researchers developed a diagnostic method based on a digital twin model by establishing a nonlinear autoregressive model for healthy PMSMs and utilizing three-phase current residuals for early ISCF diagnostics. Data-driven approaches do not require an accurate mathematical model and possess strong adaptability along with nonlinear learning capabilities.

The diagnostic methods mentioned earlier were primarily conducted under relatively stable operating conditions. However, the operating environment of wind turbines is highly uncertain, with the randomness and volatility of wind leading to instability in current and voltage. Given these limitations and the lack of robust diagnostic approaches tailored to the dynamic conditions of wind power systems, there is a pressing need to develop more reliable and adaptive fault diagnosis methods. To address these challenges, this article proposes a diagnosis method for ISCF fault in PMSGs, based on the root mean square (RMS) of stator current space vector (SCSV), a novel digital twin model (DTM), and innovative adaptive thresholds, specifically addressing the characteristics of wind fluctuations in wind power systems. The contributions and advantages of this article are as follows.

1) An innovative joint analysis of the relationship between mechanical systems and electrical systems has established a DTM model of PMSG that considers wind fluctuations.
2) By analyzing the negative correlation between the residuals of the measured RMS of SCSV and the reference values with the rate of wind variation, an adaptive threshold is designed for the first time.
3) This method is robust against wind fluctuations and minor ISCF fault, and it allows for simple construction of the DTM, enabling effective real-time diagnosis of such fault.

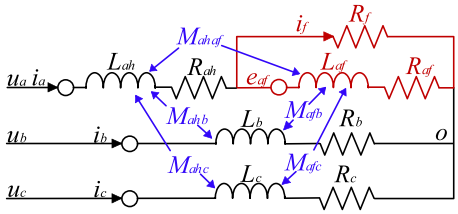

Fig. 1. ISCF fault in phase A of PMSG.

II. Diagnosis Basis for ISCF in PMSGs by RMS of SCSV

A. Mathematical Model of Healthy PMSG

The voltage equations of the direct and quadrature axes in the synchronous rotating reference frame for a healthy operation of PMSG are as follows [12]:

$$\begin{cases} u_d = R_s i_d + L_d \frac{\mathrm{d}i_d}{\mathrm{d}t} - \omega_e L_q i_q \\ u_q = R_s i_q + L_q \frac{\mathrm{d}i_q}{\mathrm{d}t} + \omega_e L_d i_d + \omega_e \psi_\mathrm{f} \end{cases} \tag{1}$$

where R_s denotes the stator resistance; ψ_f represents the magnetic flux of the permanent magnet; ω_e is the electrical angular velocity. u_d, u_q, i_d, i_q, L_d, and L_q represent the voltages, currents, and inductances of the direct and quadrature axes, respectively.

The amplitude of the SCSV I_m can be expressed as

$$I_\mathrm{m} = \sqrt{i_d^2 + i_q^2}. \tag{2}$$

B. Mathematical Model of PMSG in ISCF Fault

Taking the interturn short-circuit fault of the A-phase stator winding as an example, Fig. 1 presents an equivalent schematic diagram, it can be observed that the a-phase winding is divided into two parts: the healthy part L_{ah}, R_{ah} and the faulty part L_{af}, R_{af}. Assuming that the saturation of the generator's magnetic field is not considered, and using resistance R_f to measure the degree of insulation damage, with i_f representing the fault loop circulating current, the voltage equations for the direct and quadrature axes of the PMSG under ISCF can be expressed as follows [32]:

$$\begin{cases} u_{df} = R_s i_d + L_d \frac{\mathrm{d}i_d}{\mathrm{d}t} - \omega_e L_q i_q - \frac{2}{3} R_s \mu i_f \cos\theta \\ \qquad - \frac{2}{3} L_q \mu \frac{\mathrm{d}i_f}{\mathrm{d}t} \cos\theta - \frac{2}{3} \omega_e \mu i_f \sin\theta (L_q - L_d) \\ u_{qf} = R_s i_q + L_q \frac{\mathrm{d}i_q}{\mathrm{d}t} + \omega_e (L_d i_d + \psi_\mathrm{f}) + \frac{2}{3} R_s \mu i_f \sin\theta \\ \qquad + \frac{2}{3} L_q \mu \frac{\mathrm{d}i_f}{\mathrm{d}t} \sin\theta + \frac{2}{3} \omega_e \mu i_f \cos\theta (L_q - L_d) \end{cases} \tag{3}$$

where u_{df} and u_{qf} are the direct and quadrature axis voltages under ISCF fault; θ is the rotor position angle; μ is the ratio of the faulty turns to the total turns of the A-phase winding. By simplifying (3) according to (1), (4) can be obtained as follows:

$$\begin{cases} u_{df} = R_s i_{df} + L_d \frac{\mathrm{d}i_{df}}{\mathrm{d}t} - \omega_e L_q i_{qf} \\ u_{qf} = R_s i_{qf} + L_q \frac{\mathrm{d}i_{qf}}{\mathrm{d}t} + \omega_e i_{df} + \omega_e \psi_\mathrm{f} \end{cases} \tag{4}$$

where i_{df} and i_{qf} are the direct and quadrature axis currents under ISCF fault, with specific expressions given as follows:

$$\begin{cases} i_{df} = i_d - \frac{2}{3}\mu i_f \cos\theta_f \\ i_{qf} = i_q + \frac{2}{3}\mu i_f \sin\theta_f \end{cases} \tag{5}$$

where θ_f represents the faulty phase rotor position angle. When ISCF occur in phases a, b, and c, respectively, $\theta_f = \theta$, (θ-2/3π), (θ+2/3π).

C. Diagnosis Basis

From (2) and (5), it can be seen that when the stator experiences ISCF fault, the magnitude of the SCSV I_{mf} can be expressed as

$$\begin{aligned} I_{mf} &= \sqrt{{i_{df}}^2 + {i_{qf}}^2} \\ &= \sqrt{\left(i_d - \frac{2}{3}\mu i_f \cos\theta_f\right)^2 + \left(i_q + \frac{2}{3}\mu i_f \sin\theta_f\right)^2} \\ &= \sqrt{{I_m}^2 + \frac{4}{9}\mu^2 {i_f}^2 + \frac{4}{3}\mu i_f \left(i_q \sin\theta_f - i_d \cos\theta_f\right)}. \end{aligned} \tag{6}$$

By combining (2) and (6), the residual in the magnitude of the SCSV between the ISCF state and the healthy state of the PMSG can be expressed as follows:

$$\begin{aligned} &I_{mf} - I_m \\ &= \sqrt{{I_m}^2 + \frac{4}{9}\mu^2 {i_f}^2 + \frac{4}{3}\mu i_f (i_q \sin\theta_f - i_d \cos\theta_f)} - I_m \\ &= \frac{\frac{4}{9}\mu^2 {i_f}^2 + \frac{4}{3}\mu i_f I_m \sin(\theta_f + \phi)}{\sqrt{{I_m}^2 + \frac{4}{9}\mu^2 {i_f}^2 + \frac{4}{3}\mu i_f (i_q \sin\theta_f - i_d \cos\theta_f)} + I_m} \end{aligned} \tag{7}$$

where

$$\phi = \tan^{-1}\left(\frac{i_d}{i_q}\right). \tag{8}$$

From (7), it can be seen that when the PMSG operates under interturn short-circuit fault conditions, its SCSV magnitude I_{mf} includes an additional term for the square of the short circuit circulating current (SCCC) and a sinusoidal fluctuation term compared to the healthy state. In the absence of harmonics, the SCCC can be expressed in the following form:

$$i_f = I_f \sin(\theta_f + \theta_i) \tag{9}$$

where I_f represents the magnitude of the SCCC; θ_i denotes the initial phase angle.

Thus, substituting (9) into (7) yields

$$\begin{aligned} &I_{mf} - I_m \\ &= \frac{\frac{4}{9}\mu I_f \sin(\theta_f + \theta_i)\left[\mu I_f \sin(\theta_f + \theta_i) + \frac{3}{4} I_m \sin(\theta_f + \phi)\right]}{\sqrt{{I_m}^2 + \frac{4}{9}\mu^2 {i_f}^2 + \frac{4}{3}\mu i_f (i_q \sin\theta_f - i_d \cos\theta_f)} + I_m}. \end{aligned} \tag{10}$$

It can be seen from (10) that the ISCF fault causes the SCSV magnitude I_{mf} to exhibit a double frequency harmonic (DFH), and the harmonic amplitude primarily depends on the severity of the fault. Therefore, I_{mf} can be simplified and expressed as

$$I_{mf} = I_m \left(1 + \alpha\mu \sin(2\theta_f + \theta_{va})\right) \tag{11}$$

where α represents the amplitude coefficient of the DFH; θ_{va} denotes the initial phase angle of the DFH.

To eliminate the impact of the DFH on fault diagnosis, the RMS of I_{mf} is calculated as follows:

$$\begin{aligned} I_{mf}^{rms} &= \sqrt{\frac{1}{T}\int_0^T {I_m}^2 (1 + \alpha\mu \sin(2\theta_f + \theta_{va}))^2 dt} \\ &= \sqrt{{I_m}^2 + \frac{\alpha^2\mu^2}{2}}. \end{aligned} \tag{12}$$

Therefore, the difference in the RMS of SCSV between the ISCF state and the healthy state of the PMSG is

$$I_{mf}^{rms} - I_m^{rms} = \frac{1}{2}\frac{\alpha^2\mu^2}{\sqrt{{I_m}^2 + \frac{\alpha^2\mu^2}{2}} + I_m} \tag{13}$$

where I_m^{rms} represents the RMS of SCSV in the healthy state, which is equal to I_m.

From (13), it can be inferred that ISCF leads to a significant increase in the RMS of SCSV, and the degree of increase is positively correlated with the severity of the fault. Therefore, the RMS of SCSV can be chosen as the diagnostic variable.

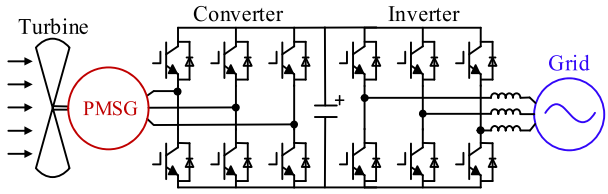

Fig. 2. Topology of PM direct-drive wind power system.

III. Digital Twin Model of PMSG in Wind Power System

The structure of the permanent magnet (PM) direct-drive wind power system is shown in Fig. 2, which includes the main components such as the wind turbine, PMSG, and full-power converter [4]. According to the analysis in Section II, ISCF fault can cause the SCSV to contain fault information. Therefore, this chapter will establish a digital twin model of the PMSG under healthy conditions to output the calculated value of the SCSV RMS for ISCF diagnosis. However, due to the complexity of wind fluctuations, the model accuracy requirements are quite high.

Compared to model-based methods such as Luenberger observers and Kalman filters, deep learning methods do not rely on model parameters and have good robustness. Thus, this chapter chooses deep learning to construct a digital twin model of PMSG in the wind power system.

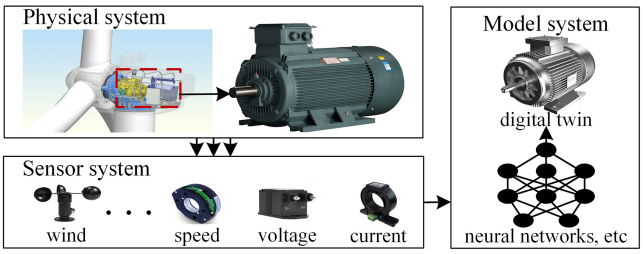

Fig. 3. PMSG digital twin modeling process.

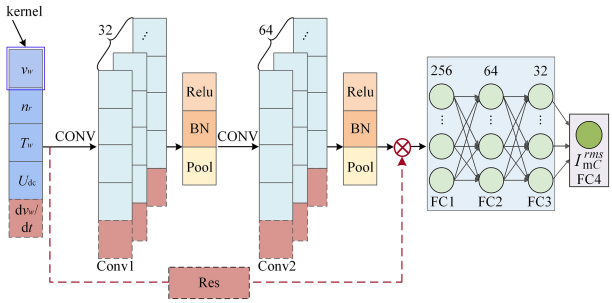

Fig. 4. PMSG digital twin model constructed by 1D-CNN.

A. Digital Twin Model of PMSG Based on Deep One-Dimensional Convolutional Neural Networks

Digital twin modeling is a popular physical system modeling technology. As shown in Fig. 3, by creating a virtual replica of the PMSG, real-time monitoring of the generator's SCSV RMS can be achieved. Neural networks, with their strong nonlinear modeling capabilities and ability to learn complex data patterns, are widely used in digital modeling applications.

In the process of model construction, the selection of input parameters is a crucial step that directly determines the accuracy of the model; these parameters should be closely related to the actual physical model. Therefore, this article will derive the expression for the nonelectrical quantities of SCSV through the joint analysis of the mechanical system and electrical system, and based on this, select the primary parameters. The electromagnetic torque T_e of the PMSG with a pole pair number of n_p can be expressed as

$$T_e = \frac{3}{2} n_p i_q \left[i_d \left(L_d - L_q \right) + \psi_{\mathrm{f}} \right]. \tag{14}$$

In fact, for PMSGs, the difference between the L_d and L_q is relatively small, and for surface-mounted generators, it holds that $L_d = L_q$. At the same time, in wind power systems, the control strategy for PMSGs is generally aimed at maximizing power generation efficiency; under this condition, i_d is much smaller than i_q, i.e., $i_d = k i_q$, where k is much less than 1. Thus, (14) can be simplified as

$$T_e = \frac{3}{2} n_p \psi_{\mathrm{f}} i_q. \tag{15}$$

The mechanical torque T_w captured by the wind turbine can be expressed as

$$T_w = \frac{\rho \pi R^2 v_w^3 C_p}{2\omega} \tag{16}$$

where ρ represents air density, R is the radius of the wind turbine blades, v_w denotes wind speed, C_p is the wind energy utilization coefficient, and ω is the rotational angular velocity of the turbine.

Furthermore, the T_w transmitted from the wind turbine to the PMSG generates iron loss torque, mechanical loss torque, and stray loss torque. By summing these torques, the generator's loss torque T_{loss} can be obtained

$$T_{\mathrm{loss}} = C_1 + C_2 \omega \tag{17}$$

where C_1 represents the sum of the constant part of iron loss, mechanical loss, and stray loss, while C_2 denotes the coefficient of the variable part of the iron loss.

According to the law of conservation of momentum, the T_w should equal the sum of the T_e and the T_{loss}, i.e.,

$$T_w = T_e + T_{\mathrm{loss}}. \tag{18}$$

Substituting (15), (16), and (17) into (18) gives the expression for the SCSV magnitude

$$\begin{aligned} I_m &= \sqrt{i_d^2 + i_q^2} = \sqrt{k^2 i_q^2 + i_q^2} = \sqrt{1 + k^2} \cdot i_q \\ &= \sqrt{1 + k^2} \frac{\rho \pi R^2 v_w^3 C_p - 2(C_1 \omega + C_2 \omega^2)}{3 \omega n_p \psi_{\mathrm{f}}}. \end{aligned} \tag{19}$$

From (19), it can be seen that the SCSV magnitude is primarily related to wind speed and rotational speed (angular velocity) among nonelectrical quantities. Therefore, this article chooses v_w and rotational speed n_r as the main input parameters for the model, and selects mechanical torque T_w and dc bus voltage U_{dc} as auxiliary input parameters.

Compared to traditional fully connected neural networks, 1D-CNN can reduce the number of training parameters through local connections and weight sharing, thereby improving computational efficiency and making them suitable for large-scale PMSG data processing [33]. In addition, the processing through convolutional layers gives 1D-CNN a certain robustness against noise interference. Thus, this article adopts a deep 1D-CNN to construct the digital twin model of PMSG, as shown in the solid line section of Fig. 4. The main structure of the model consists of multichannel 1-D convolutional layers and fully connected layers. The input parameters are $X = \{v_w, n_r, T_w, U_{\mathrm{dc}}\}$, and the output is the calculated value of the RMS of SCSV $Y = I_{\mathrm{mC}}^{\mathrm{rms}}$.

The mathematical relationship between output Y and input X, which represents the forward propagation process of the neural network, can be approximately expressed as

$$Y = f(X; \beta) \tag{20}$$

where f is the nonlinear mapping function learned by the 1D-CNN. β represents the parameters of the model, which include the weights and biases in the convolutional layers and fully connected layers.

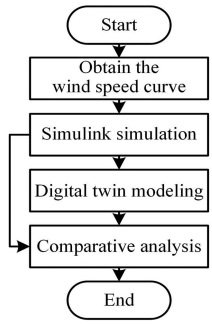

Fig. 5. Validation process of digital twin model.

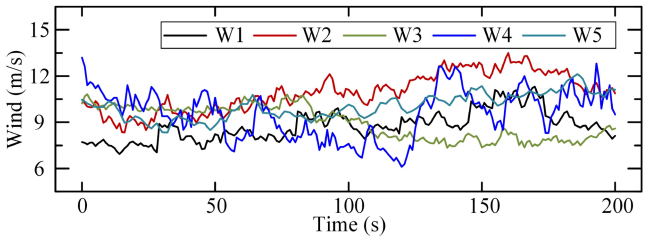

Fig. 6. Typical wind speed waveform curve.

By expanding (20), a more detailed expression can be obtained as follows:

$$I_{mC}^{rms} = F_{4\_1}\left(R_2\left(C_2\left(R_1\left(C_1\left(\{V_w, N_r, T_w, U_{dc}\}\right)\right)\right)\right)\right) \quad (21)$$

where F_{4_1} denotes the transformation of the last four fully connected layers; R_1 and R_2 denote the first and second activation, batch normalization, and pooling operations, respectively; C_1 and C_2 refer to the convolutional processes of the first and second layers (Conv1-2).

In which the core operation of the 1-D convolution operation C can be represented as

$$C(x) = \begin{bmatrix} \sum_{j=0}^{l-1} x[1\cdot s + j + p]\cdot w[j] \\ \sum_{j=0}^{l-1} x[2\cdot s + j + p]\cdot w[j] \\ \vdots \\ \sum_{j=0}^{l-1} x[m\cdot s + j + p]\cdot w[j] \end{bmatrix} \quad (22)$$

where the input signal x has the dimension $n\times 1$, the convolution kernel w has the dimension $l\times 1$, with a kernel size of l, stride s, and padding p. The output signal $C(x)$ has the dimension $m\times 1$, and m can be calculated using the following formula:

$$m = \frac{n + 2p - l}{s} + 1. \quad (23)$$

B. Digital Model Verification and Analysis

To validate the digital model of the PMSG presented in the previous section, simulations have been conducted using MATLAB/ Simulink, as shown in Fig. 5. The process involves four steps as follows.

Step 1: Obtain the typical wind speed curves W1-5 for offshore wind turbines, each lasting 200 s, as illustrated in Fig. 6.

TABLE I
PARAMETERS OF THE PMSG

Parameters	Values
Rated Power/W	550
Rated Voltage/V	380
Phase resistance/Ω	10.5
Inductor/H	0.16
Pairs of poles	2
Permanent flux linkage/Wb	0.636

TABLE II
HYPERPARAMETERS OF THE DIGITAL TWIN MODEL

Layer	Output size	Kernel	Padding	Stride
Conv1	(32,1,4)	1	1	0
Conv2	(64,1,4)	1	1	0
FC1	(256,1)	/	/	/
FC2	(64,1)	/	/	/
FC3	(32,1)	/	/	/
FC4	(1,1)	/	/	/

Step 2: Use MATLAB/Simulink to model the PMSG in the wind power system, as shown in the upper part of Fig. 12. The wind turbine calculates reference torque and speed based on the input v_w. The reference torque serves as the load torque, while the reference speed is utilized in a dual closed-loop control strategy. A zero d-axis current vector control strategy is employed, and a proportional-integral (PI) controller generates the reference voltage, leading to the space vector PWM switching method for closed-loop control of the PMSM.

The parameters of the simulation motor model are consistent with those of the experimental platform, as detailed in Table I. The simulation collects the dataset $\{X, Y\}$ needed for the twin model under wind speed curves W1-5, sampling 2500 times per second, resulting in a total of 2 million cleaned data samples.

Step 3: Based on the digital model of the PMSG presented in the preceding section and the dataset obtained in Step 2, modeling and training will be carried out using Python/PyTorch. The model is implemented using the PyTorch 3.12 framework in a Python 3.9 environment, with the computer's CPU and GPU being an AMD Ryzen 9 7845HX and an RTX 4060 @ 8 GB, respectively.

The dataset is randomly divided into a training set and a test set in an 8:2 ratio after cleaning, with no overlap between the two. During the training process, the Adam optimizer is used for optimization, and the initial learning rate is set to 0.0001. The loss function used is the mean squared error, with a batch size set to 64, and the model training is completed after 50 iterations. Table II lists the main hyperparameters of the model after adjustment with the test set. Fig. 7(a) shows the loss curves of the model on the training and test sets, and Fig. 7(b) shows the comparison between the normalized model's calculated values I_{mC}^{rms} and the measured values I_{mM}^{rms} of the RMS of SCSV.

Step 4: Perform a comparative analysis of the simulation model and the twin model using the test wind. This wind is extracted from a 50s segment with significant fluctuations from W1-5 and is repeated once. The specific waveform is presented

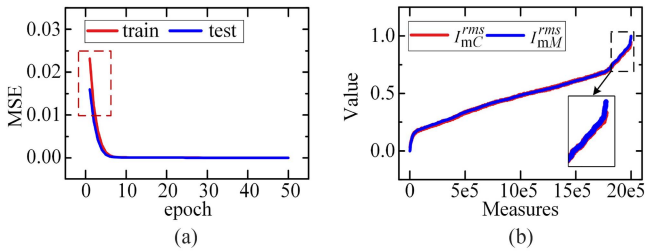

Fig. 7. Loss curve and comparison chart of model calculated values versus measured values. (a) Loss curve. (b) calculated and measured value.

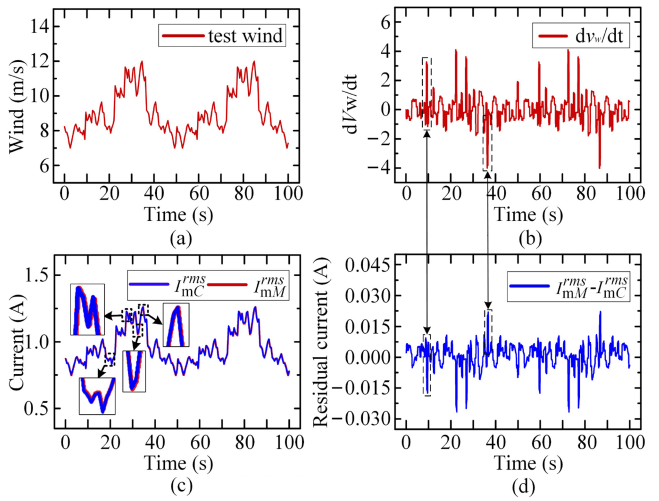

Fig. 8. Comparison of simulation and 1D-CNN digital twin model. (a) Wind speed curve. (b) Wind variation rate curve. (c) RMS of SCSV curve. (d) Residual current curve.

in Fig. 8(a), while the wind variation rate curve is shown in Fig. 8(b). A synchronous simulation comparison of the simulation model and the digital model is conducted in Simulink, with the comparison and residual curves of $I_{\mathrm{m}M}^{\mathrm{rms}}$ and $I_{\mathrm{m}C}^{\mathrm{rms}}$ displayed in Fig. 8(c) and (d).

From Fig. 8(a), (c), and (d), it is clear that the digital twin model effectively tracks the output of the PMSG under wind speed fluctuations, with the absolute residual not exceeding 0.03. Moreover, Fig. 8(b) and (d) shows a negative correlation between the residual curve and the wind speed variation rate; as the wind speed variation rate increases, the difference decreases, and vice versa.

C. PMSG Digital Twin Model With Wind Speed Variation Rate

In the previous section, the accuracy of the digital model was validated, revealing a strong correlation between its precision and the wind variation rate. To further enhance the accuracy of the digital twin model, this section incorporates the wind variation rate $\mathrm{d}v_w/\mathrm{d}t$ as an input parameter and introduces a residual (Res) structure to mitigate potential overfitting resulting from increased model complexity. The improved model structure is illustrated in the dashed section of Fig. 4.

Following the validation steps from the Fig. 5, the improved model underwent simulation verification. Fig. 9(a) and (b)

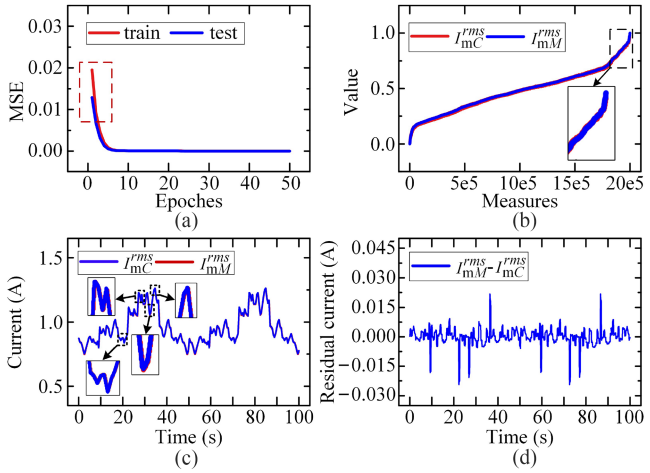

Fig. 9. Results of the improved model. (a) Loss curve. (b) Calculated and measured value. (c) RMS of SCSV curve. (d) Residual current curve.

TABLE III
COMPARISON OF MSE BEFORE AND AFTER IMPROVEMENT

MSE	$\mathrm{d}v_w/\mathrm{d}t$	No $\mathrm{d}v_w/\mathrm{d}t$	*Improvement* (%)
LSMT	1.0926e-05	2.3167e-05	52.84
OD	1.2805e-05	2.4909e-05	48.59
TWS	2.8874e-05	3.7374e-05	22.74

presents the loss curves for the training and testing sets, along with a normalized comparison of the $I_{\mathrm{m}C}^{\mathrm{rms}}$ against $I_{\mathrm{m}M}^{\mathrm{rms}}$. Fig. 9(c) and (d) shows the comparison curves between $I_{\mathrm{m}M}^{\mathrm{rms}}$ and $I_{\mathrm{m}C}^{\mathrm{rms}}$ at the test wind speed, along with the residual curves

$$\text{Improvement}(\%) = \left(\frac{\text{MSE}_{\text{Old}} - \text{MSE}_{\text{New}}}{\text{MSE}_{\text{Old}}}\right) \times 100\%. \quad (24)$$

The improved model demonstrates a significant decrease in loss for both the training and testing sets. While the residual curves have improved, they still show a strong negative correlation with the wind speed variation rate. Table III details the mean squared error (MSE) between the calculated and measured values of the RMS of SCSV for the last step of model training (LSMT), the overall dataset (OD), and the test wind speed (TWS), both before and after introducing the wind speed variation rate. It also presents the percentage improvement in performance, calculated according to (24). The results clearly indicate that incorporating the wind variation rate significantly enhances model performance.

IV. DIAGNOSIS STRATEGY BASED ON ADAPTIVE THRESHOLDS

Based on the research from the previous two chapters, this chapter designs a diagnosis strategy for ISCF fault in PMSGs based on adaptive thresholds, as shown in Fig. 10. First, the SCSV RMS of the generator $I_{\mathrm{m}M}^{\mathrm{rms}}$ is measured in real time, and a digital model is used to calculate the reference value $I_{\mathrm{m}C}^{\mathrm{rms}}$ under the same operating conditions, thereby obtaining the residual between the two. Next, based on the adaptive threshold proposed in Section IV-C, the diagnosis of whether the generator has an ISCF

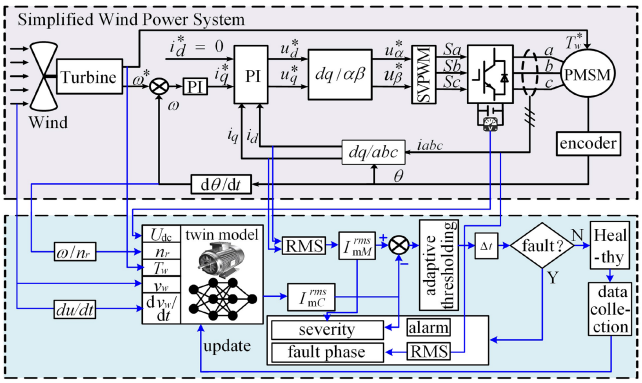

Fig. 10. ISCF fault diagnosis structure.

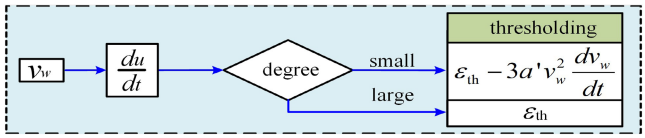

Fig. 11. Adaptive threshold block diagram.

fault is performed. To improve the accuracy of fault diagnosis, a time window Δt is set; the generator is considered to have an ISCF fault only if the duration during which the residual exceeds the adaptive threshold within the time window exceeds $\Delta t/2$. Otherwise, the generator is deemed to be operating normally.

During normal generator operation, the digital twin model employs an online update mechanism to dynamically integrate operational data, compensating for parameter drift caused by aging effects such as winding insulation degradation. The retraining frequency and maintenance strategy are adaptively adjusted based on the generator's aging rate and operational load characteristics. In the event of ISCF fault, the system performs fault phase localization and severity assessment, followed by the issuance of an alarm signal to prompt timely maintenance actions.

A. *Adaptive Threshold Based on the Rate of Wind Variation*

Analysis in Section IV-C shows that the SCSV RMS residual is negatively correlated with the rate of wind variation. When the wind fluctuates significantly, the current residual also experiences substantial reverse fluctuations. Furthermore, as indicated by (13), the residual is positively correlated with fault severity. Thus, when the severity of a ISCF fault is low and wind fluctuates greatly, the residual fluctuations in normal and fault conditions significantly overlap, hindering fault diagnosis. Therefore, this section will explore the reasons for the negative correlation between current residuals and the wind variation rate and design an adaptive threshold to enhance fault diagnosis accuracy.

PM direct-drive wind power systems generally operate in a low-speed state, with limited variation in ω, allowing (19) to be simplified to

$$I_m = a_1 v_w^3 - a_2 \tag{25}$$

where a_1 and a_2 are treated as approximately constant values that characterize the relationship between SCSV and the cube of wind speed, with their specific formulations shown in (26) and (27), respectively, as follows:

$$a_1 = \sqrt{1+k^2}\frac{\rho\pi R^2 C_p}{3\omega n_p \psi_{\mathrm{f}}} \tag{26}$$

$$a_2 = \sqrt{1+k^2}\frac{2(C_1\omega + C_2\omega^2)}{3\omega n_p \psi_{\mathrm{f}}}. \tag{27}$$

Under conditions of wind fluctuations, to further consider the smoothing effect of PI controller and rotational inertia on I_{m}, it can be expressed as

$$\begin{aligned} I_m &= a_1 v_w^3 - a_2 - a'\frac{dv_w^3}{dt} \\ &= a_1 v_w^3 - a_2 - 3a' v_w^2 \frac{dv_w}{dt} \end{aligned} \tag{28}$$

where a' represents the level of smoothing of I_{m} by the PI controller and rotational inertia under conditions of wind fluctuations, with its value estimated to be between $0.01a_1$ and $0.1a_1$.

The digital model of the PMSG for modeling the SCSV RMS that under steady wind conditions, the error compared to measured values remains approximately constant at a small value ε. However, in wind fluctuations, limited data due to sharp fluctuations, along with increased model complexity from PI and rotational inertia, makes it challenging to accurately capture the true physical model of the wind turbine during significant wind speed changes. Consequently, under these fluctuations, the residuals primarily vary with the rate of wind change

$$\begin{aligned} I_{\mathrm{m}M}^{\mathrm{rms}} - I_{\mathrm{m}C}^{\mathrm{rms}} &= a_1 v_w^3 - a_2 - 3a' v_w^2 \frac{dv_w}{dt} - I_{\mathrm{m}C}^{\mathrm{rms}} \\ &= \varepsilon - 3a' v_w^2 \frac{dv_w}{dt}. \end{aligned} \tag{29}$$

Therefore, the threshold values for fault diagnosis variables during slight interturn short-circuit fault should also change with the rate of wind variation as follows:

$$I_{\mathrm{th}} = \varepsilon_{\mathrm{th}} - 3a' v_w^2 \frac{dv_w}{dt} \tag{30}$$

where I_{th} represents the threshold for the SCSV RMS residual, while $\varepsilon_{\mathrm{th}}$ indicates the threshold for the residual under steady wind conditions.

The adaptive threshold block diagram is shown in Fig. 11. When the degree of wind variation rate is small, the diagnostic variable threshold is chosen as $\varepsilon_{\mathrm{th}}$, otherwise the threshold is selected as $\varepsilon_{\mathrm{th}} - 3a' v_w^2 dv_w/dt$. Specifically, in the subsequent experiments of this article, $\varepsilon_{\mathrm{th}} = 0.012$, a' = 5e-4.

B. *Faulty Phase Localization Strategy*

When ISCF fault occurs in PMSGs, the short-circuit resistance provides an additional low-impedance path for the current, resulting in an even more significant increase in the RMS of current flowing through the faulty phase compared to the other two phases. Therefore, the localization of the faulty phase can be

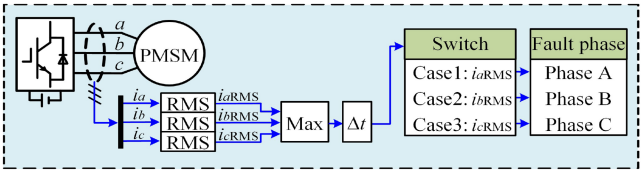

Fig. 12. Faulty phase localization strategy diagram.

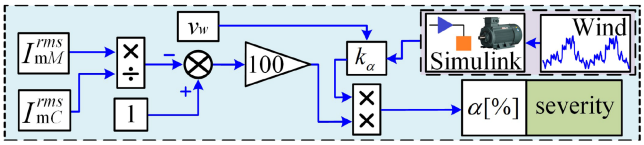

Fig. 13. ISCF fault severity estimation diagram.

performed by measuring the RMS of the three-phase currents, as shown in Fig. 12. The maximum RMS of the three-phase currents are determined using the Max function. To improve the accuracy of faulty phase localization, a time window $\Delta t$is designed to output only the maximum current value that occupies the largest proportion within $\Delta t/2$ time. Finally, the phase corresponding to the maximum current value is identified as the faulty phase.

In addition, while the RMS of the three-phase currents can be used for faulty phase localization, they are not suitable for direct fault diagnosis. This is because, in practical systems, the three-phase windings of PMSG are not perfectly symmetrical, and there is always a phase with a slightly higher current RMS under normal conditions. This inherent asymmetry can easily lead to misdiagnosis. Furthermore, the SCSV RMS is typically much larger than that of a single-phase current RMS, which can result in slower and less distinct fault detection.

C. Severity Estimation Method

According to (13), an ISCF fault will increase the RMS of SCSV, and the extent of this increase is positively correlated with the severity of the fault. Therefore, the severity can be estimated through the RMS of SCSV [34]. The specific formula is as follows:

$$\alpha[\%] = \frac{N_{\text{fail}}}{N_{total}} \cdot 100 = k_\alpha(v_w) \cdot \left(1 - \frac{I^{\text{rms}}_{\text{m}M}}{I^{\text{rms}}_{\text{m}C}}\right) \cdot 100 \quad (31)$$

where N_{fail} represents the number of faulty turns, N_{total} denotes the total number of turns, and $k_\alpha(v_w)$ refers to the wind speed correlation coefficient. This coefficient is introduced to enhance the accuracy of the severity estimation, and its value is derived through simulation fitting.

Fig. 13 shows the block diagram of the severity estimation method for ISCF fault in PMSGs. In the actual system, the specific value of the wind speed correlation coefficient is derived by combining the measured wind speed with simulation fitting, allowing the estimation of ISCF fault severity based on (31).

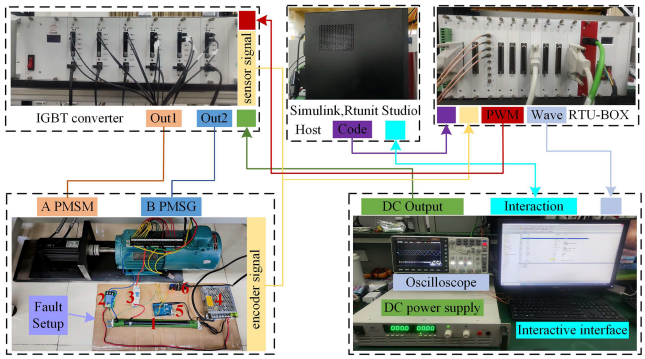

Fig. 14. Experimental platform.

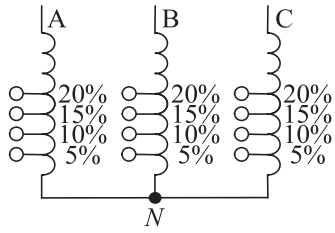

Fig. 15. Short-circuit terminal of stator winding.

V. Experimental Verification

A. Platform

To validate the effectiveness of the method proposed in this article, an experimental platform for a PM direct-drive wind power system was established. As illustrated in Fig. 14, the platform comprises several key components: the A PMSM simulates the wind turbine by providing load torque based on wind speed, while the B PMSG simulates the generator with speed tracking control. The parameters of the PMSG align with those used in the simulations in Section III. The converter features IGBT integrated modules from Rtunit, and the controller employs the RTU-BOX real-time simulation system, which connects to the MATLAB/Simulink environment. By compiling the Simulink model, code that the RTU-BOX can recognize is generated, enabling the creation of an experimental system through Rtunit Studio that allows online adjustment of various parameters.

In this experimental setup, the PMSG acts as the test motor, featuring terminal connections on its three-phase stator winding for interturn short-circuits at 5%, 10%, 15%, and 20%, as shown in Fig. 15. Each phase coil consists of a total of 460 turns. The fault configuration includes: 1) slide rheostat, 2) relay, 3) air switch, 4) switching power supply, 5) microcontroller, and 6) RS485 communication cable. When the air switch is closed, the fault signal from Rtunit Studio is sent to the microcontroller via the RS485 cable. The microcontroller then activates the relay to connect the slide rheostat to the interturn short-circuit loop, with both the microcontroller and relay powered by the switching power supply.

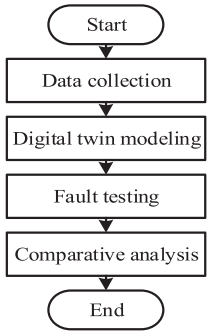

Fig. 16. Process for experimental verification.

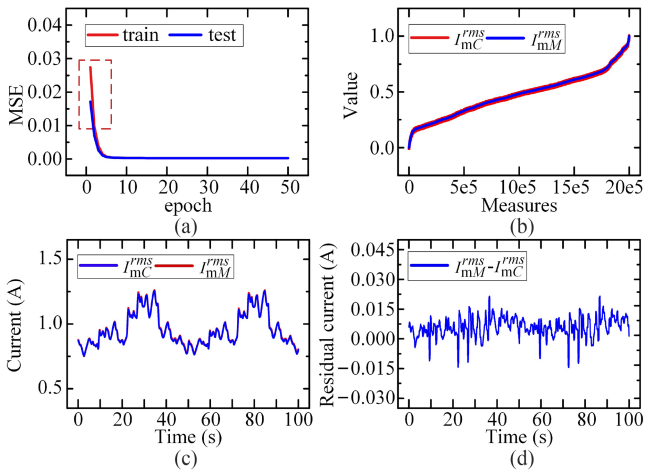

Fig. 17. Performance of digital twin model in experiments. (a) Loss curve. (b) Calculated and measured value. (c) RMS of SCSV curve. (d) Residual current curve.

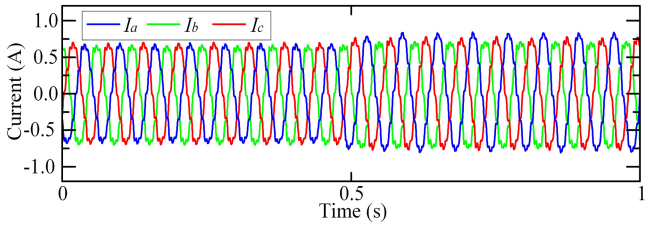

Fig. 18. Three-phase current waveform of PMSG before and after ISCF10%.

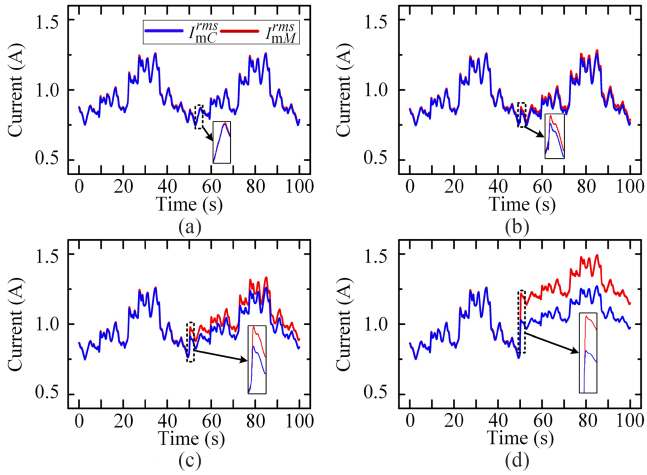

Fig. 19. SCSV RMS under Health, ISCF5%, ISCF10%, and ISCF20%. (a) Health. (b) ISCF5%. (c) ISCF10%. (d) ISCF20%.

B. Verification and Analysis

The verification process is illustrated in Fig. 16 and consists of four steps.

Step 1. Data collection: Based on the wind speed curve W1-5 shown in Fig. 6, the wind power system simulation control program is run on the experimental platform. The A PMSM simulates the wind turbine, providing load torque according to the wind speed, while the PMSG simulates the generator, implementing speed tracking control based on wind speed. During the experiment, 2500 times sampled per second, and after cleaning, a dataset containing 2.00 million samples is created, labeled as $\{X, Y\}$.

Step 2. Digital twin modeling: Based on the PMSG digital model introduced in Section III-C, which incorporates the wind speed variation rate, and the digital modeling methods outlined in Step 3 of Section III-B, the dataset collected in Step 1 is used to create a digital model of the PMSG in the experimental platform. Fig. 17(a) and (b) shows the loss curves of the model on the training and testing sets, as well as a normalized comparison between the model's calculated values and the actual measured values. The comparison curves for $I_{\mathrm{m}M}^{\mathrm{rms}}$ and $I_{\mathrm{m}C}^{\mathrm{rms}}$ under the test wind, along with the residual curves, are illustrated in Fig. 17(c) and (d). Furthermore, the model exhibits a size of 23.01 KB, an inference time of 0.4762 ms, a memory consumption of 0.12 KB, which meets the requirements for real-time diagnosis.

From Fig. 17, it can be concluded that the PMSG digital model, which incorporates the wind speed variation rate, still demonstrates good accuracy in the actual experimental system. Furthermore, the residuals between the measured values of the RMS of SCSV and the calculated values of the digital model exhibit a strong negative correlation with the wind variation rate, suggesting its potential for use in fault diagnosis systems.

Step 3. Fault testing: The fault testing verifies the performance of the diagnosis system under four different conditions: health and ISCF faults in the A-phase stator winding at 5% (ISCF5%), 10% (ISCF10%), and 20% (ISCF20%). The tests are conducted under the test wind, and at the 50-s mark, the relay is closed, connecting the slide rheostat to the fault loop. Additionally, based on the principle of parallel resistance and the fact that the resistance of the motor windings is very low, it is understood that the value of the fault resistance has a minimal effect on the characteristics of ISCF fault. Thus, the fault resistance value is set to $R_f = 3\ \Omega$.

Fig. 18 shows the three-phase current waveform with a constant wind speed of 9 m/s, and an ISCF10% fault on phase A occurring after 0.5 s. It can be seen that after the fault occurs, the amplitude of the fault phase current increases and the degree of asymmetry becomes more pronounced.

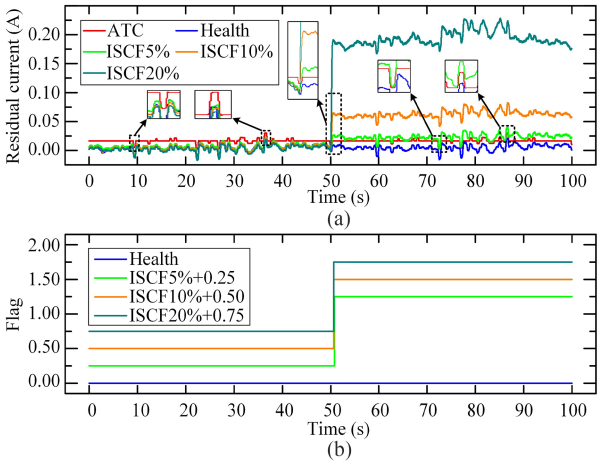

Fig. 20. Residual of SCSV RMS and fault indicator under Health, ISCF5%, ISCF10%, and ISCF20%. (a) $I_{\mathrm{m}M}^{\mathrm{rms}}$ - $I_{\mathrm{m}C}^{\mathrm{rms}}$. (b) Fault indicator.

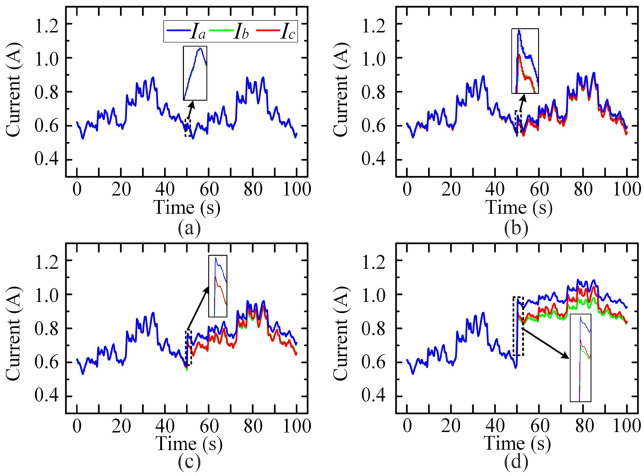

Fig. 21. Three-phase current RMS of PMSG under Health, ISCF5%, ISCF10%, and ISCF20%. (a) Health. (b) ISCF5%. (c) ISCF10%. (d) ISCF20%.

Fig. 19 shows the comparison between the measured and calculated values of the SCSV RMS under four operating conditions. It can be observed that the residuals between them increase as the degree of ISCF fault severity grows. Fig. 20 illustrates the SCSV RMS residuals and fault indicators under the four conditions, with ATC representing the adaptive threshold curve based on the wind variation rate. It can be seen that during slight ISCF fault, the adaptive threshold effectively eliminates the impact of wind fluctuations on fault diagnosis, especially in the case of slight fault. Moreover, the time taken to diagnose ISCF5%, ISCF10%, and ISCF20% faults occurring at 50 s is 0.541 s, 0.386 s, and 0.230 s, respectively, which meets the requirements for fault detection.

Fig. 21 shows the RMS of three-phase currents under four operating conditions. Under healthy conditions, the RMS of the three-phase currents are basically equal. When an ISCF occurs in one phase, the RMS of the three-phase currents increase with the severity of the fault; however, the current increase in the faulted phase is more pronounced, allowing for fault phase localization.

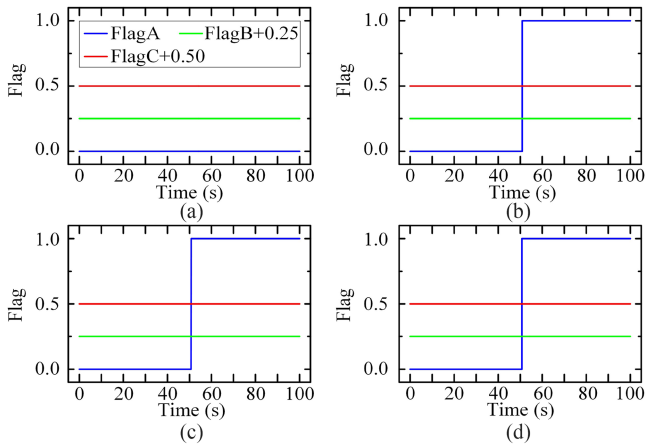

Fig. 22. Faulty phase localization indicator under Health, ISCF5%, ISCF10%, and ISCF20%. (a) Health. (b) ISCF5%. (c) ISCF10%. (d) ISCF20%.

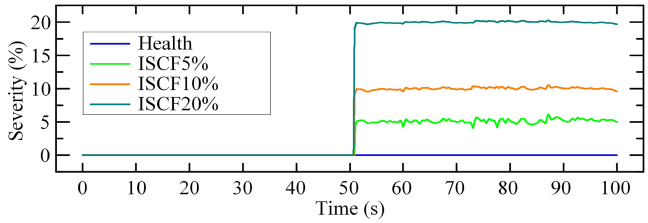

Fig. 23. Fault severity estimation under Health, ISCF5%, ISCF10%, and ISCF20%.

As shown in Fig. 22, after a fault occurs at 50 s, the phase A localization indicator jumps from 0 to 1, indicating that a ISCF has occurred in the phase A winding. Fig. 23 shows the estimation of ISCF severity. It can be observed that after the fault occurs at 50 s, the method proposed in this article effectively estimates the severity, with accuracy increasing as the severity rises. Additionally, this method performs effectively even under wind fluctuations.

C. Robustness Verification

To further validate the robustness of the proposed method, this article conducted a series of tests, including noise interference testing, varying wind speed testing, sudden wind speed change testing, and different fault resistance testing.

The noise interference test was conducted by introducing Gaussian white noise into the current signals. Fig. 24 demonstrates the diagnostic system's performance in identifying ISCF5% in phase A under a signal-to-noise ratio of 20 dB. As observed, the system accurately diagnoses the fault, locates the faulty phase, and estimates the severity level even when the fault occurs at 50 s. This reliability is primarily attributed to the inherent noise resistance of the three-phase current RMS values and the effective filtering mechanisms integrated into the diagnostic system.

Subsequently, the diagnostic system was evaluated under two distinct wind conditions (wind1 and wind2). Consistent with the previous experimental setup, the wind speed remained constant

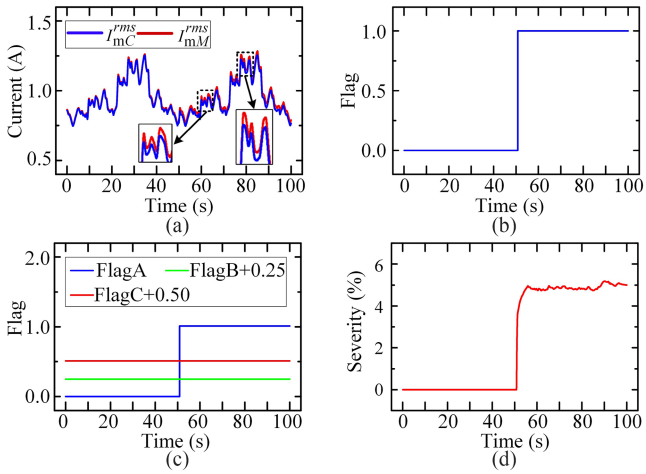

Fig. 24. Noise interference test under ISCF5%. (a) RMS of SCSV curve. (b) ISCF flag. (c) Faulty phase flag. (d) Severity estimation.

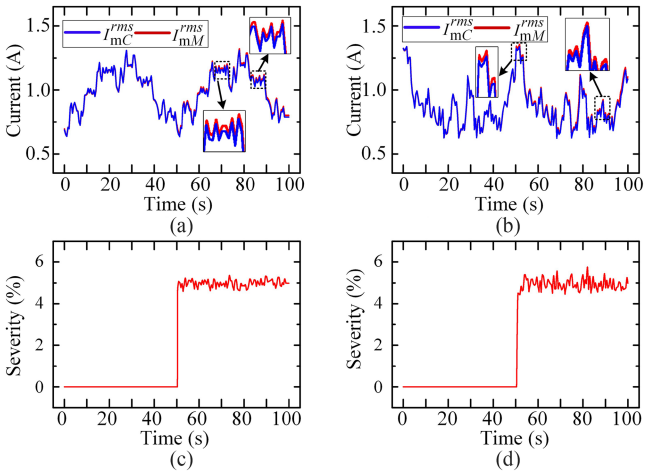

Fig. 25. Diagnosis effectiveness of ISCF5% under different wind conditions.(a) RMS of SCSV curve. (b) RMS of SCSV curve. (c) Severity estimation. (d) Severity estimation.

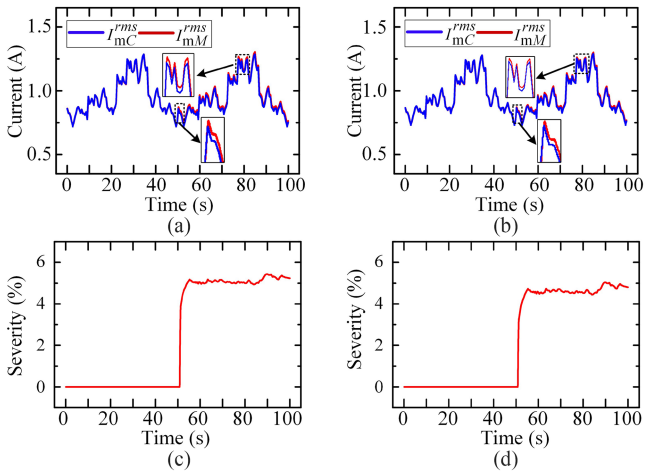

Fig. 26. Diagnosis effectiveness of ISCF5% under different R_f. (a) RMS of SCSV curve. (b) RMS of SCSV curve. (c) Severity estimation. (d) Severity estimation.

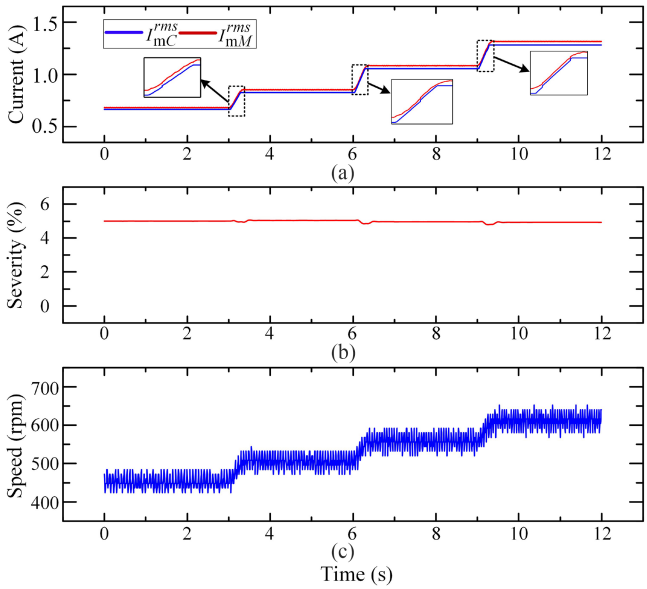

Fig. 27. Effectiveness of ISCF5% diagnosis under wind transients. (a) RMS of SCSV curve. (b) Severity estimation. (c) Speedy curve.

throughout the first 50 s, followed by the introduction of an ISCF5% in phase A at the 50s mark. While the wind speed waveform pattern is similar to the SCSV RMS waveform and, thus, not shown separately, the system's performance is clearly demonstrated through the following results: Fig. 25(a) and (c) presents the SCSV RMS comparison curve and severity estimation curve, respectively, for wind1 conditions, while Fig. 25(b) and (d) shows the corresponding curves for wind2. The experimental results indicate that the diagnostic system maintains consistent and reliable performance across different wind speed conditions.

Furthermore, this study validates the diagnostic performance of the proposed method under varying R_f Fig. 26(a) and (c) presents the SCSV RMS curve and severity estimation curve, respectively, for a ISCF5% in phase A occurring at 50 s under test wind speed with $R_f = 1\ \Omega$. Correspondingly, Fig. 26(b) and (d) illustrates the same metrics under identical fault conditions but with $R_f = 5\ \Omega$. The results demonstrate that while the severity estimation values tend to be slightly higher at lower R_f and marginally lower at higher R_f, these variations have minimal impact on the overall fault diagnosis accuracy.

Finally, this article evaluates the transient performance of the diagnostic system by simulating abrupt wind changes under a ISCF5%. The wind speed profile is set as follows: constant at 6 m/s (0–3 s), linearly increasing to 8 m/s (3.0–3.25 s), constant at 8 m/s (3.25–6.0 s), linearly increasing to 10 m/s (6.0–6.25 s), constant at 10 m/s (6.25–9 s), linearly increasing to 12 m/s (9.0–9.25 s), and constant at 12 m/s thereafter. Fig. 27(a) presents the SCSV RMS comparison curve during this process, Fig. 27(b) illustrates the severity estimation, and Fig. 27(c) shows the rotational speed curve. The results reveal that although the severity estimation experiences a slight decline

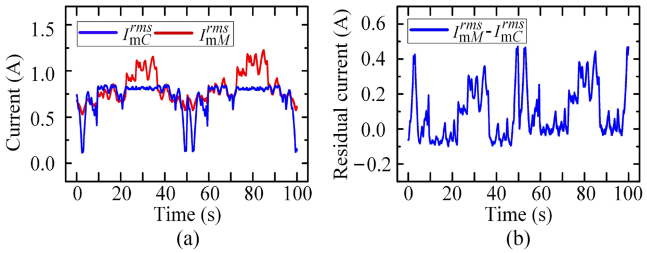

Fig. 28. Luenberger observer performance under ISCF10%.(a) RMS of SCSV curve. (b) Residual current curve.

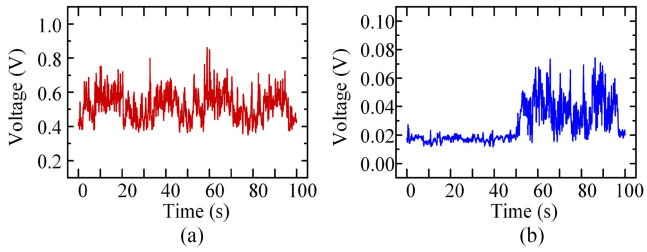

Fig. 30. Zero-sequence voltage fundamental amplitude curve. (a) V_0 fundamental amplitude. (b) $V_{0\mathrm{m}}$ fundamental amplitude

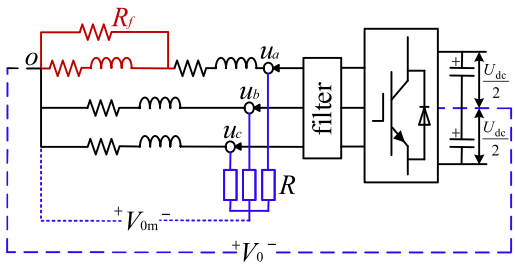

Fig. 29. Zero-sequence voltage measurement diagram.

TABLE IV
COMPARISON OF COMMON ISCF DIAGNOSIS METHODS

Methods	TL	RB	DQR	PD	FDL	SE
Model-based methods [16-20]	good	poor	low	high	yes	no
Signal analysis methods [21-25]	good	poor	low	high	yes	no
Data-driven methods [26-28,30-31]	poor	good	high	low	yes	yes
The proposed method	good	good	low	low	yes	yes

during wind speed transitions, the diagnostic system maintains robust and effective performance throughout the abrupt changes, demonstrating its reliability under dynamic conditions.

D. Comparison of Different Methods

To analyze the advantages and limitations of the method proposed in this article compared to traditional fault diagnosis methods, the focus is on the robustness (wind fluctuations) of the observer-based method and the zero-sequence voltage method.

The method based on the Luenberger observer demonstrates the measured value $I_{\mathrm{m}M}^{\mathrm{rms}}$, the estimated value $I_{\mathrm{m}C}^{\mathrm{rms}}$, and the residuals between the two under test wind, as illustrated in Fig. 28. When the wind is stable and within the mid-range, the observer is able to barely track the actual value of SCSV RMS. However, during wind fluctuations, a significant difference between the observed and measured values becomes evident. Although the magnitude of the difference increases after the occurrence of the ISCF10% at the 50 s, the distinction is not clear, rendering it unsuitable as a variable for diagnosis.

The zero-sequence voltage method generally relies on the characteristic of the fundamental zero-sequence voltage being sensitive to faults. As shown in Fig. 29, the voltage measured between the dc midpoint of the inverter and the center of the stator winding is the zero-sequence voltage V_0. However, V_0 can be easily affected by the converter. To eliminate this influence, using a three-phase balanced resistor network to measure the zero-sequence voltage $V_{0\mathrm{m}}$, which is less susceptible to the converter's effects.

Fig. 30(a) and (b) shows the fundamental amplitude curves of V_0 and $V_{0\mathrm{m}}$ at the test wind, with an ISCF5% occurring after the 50th s. It can be seen that although the balanced $V_{0\mathrm{m}}$ shows a significant response to the fault, its robustness is poor under wind fluctuations.

At the same time, this article compares several important indicators, such as timeliness (TL), robustness (RB), data quality requirements (DQRs), parameter dependency (PD), fault detection and localization (FDL), and severity estimation (SE), for common ISCF fault diagnosis methods, with the results shown in Table IV. It can be observed that the proposed method demonstrates good robustness and effective capabilities in fault detection, localization, and severity assessment, while other methods have one or more shortcomings. In addition, the methods employed in this study are indeed data-driven, relying on historical operational data to train the digital twin model for fault diagnosis. However, unlike the deep learning-based methods referenced in Table IV, which primarily focus on classification tasks, the proposed approach emphasizes model-based fault diagnosis by integrating physical insights with data-driven techniques. This hybrid approach not only enhances interpretability but also ensures robust performance under varying operational conditions.

VI. CONCLUSION

This article proposes a method for localization and severity estimation of ISCF fault in PMSGs within wind power systems, based on SCSV RMS, digital twin models, and adaptive thresholds. Simulations and experiments have validated the effectiveness of the proposed method, leading to the following conclusions.

1) ISCF fault causes a significant increase in the SCSV RMS, and the degree of increase is positively correlated with the severity of the fault. The RMS of the fault phase current shows a greater increase compared to the normal two phases. Based on this, fault detection, localization, and severity estimation are achieved.

2) By jointly analyzing the mechanical and electrical systems, a nonelectrical expression for SCSV is derived. Key parameters are selected accordingly to establish a digital model of the PMSG. Simulations reveal a negative correlation between the SCSV RMS residual and the rate of wind variation, leading to the incorporation of the wind variation rate into the digital model, further enhancing its accuracy.
3) The reasons for the negative correlation between the SCSV RMS residual and the wind change rate are analyzed, and an adaptive threshold based on the wind variation rate is designed, effectively enabling the diagnosis of minor faults.

Future research will focus on further improving the accuracy and transferability of the digital twin model. Additionally, the application of the proposed method to open-circuit fault diagnosis will be explored, extending its applicability to a broader range of fault scenarios in wind power systems.

REFERENCES

[1] R. Tan, Z. Jing, Y. Wang, and Z. Zhao, "An effective scheduling strategy for offshore wind farm maintenance optimization considering multi-practical operation conditions," *Protection Control Modern Power Syst.*, vol. 10, no. 2, pp. 133–149, Mar. 2025.

[2] P. Roy, J. He, T. Zhao, and Y. V. Singh, "Recent advances of wind-solar hybrid renewable energy systems for power generation: A review," *IEEE Open J. Ind. Electron. Soc.*, vol. 3, pp. 81–104, 2022.

[3] Y. Cao et al., "Life cycle environmental analysis of offshore wind power: A case study of the large-scale offshore wind farm in China," *Renewable Sustain. Energy Rev.*, vol. 196, May 2024, Art. no. 114351.

[4] Y. Zhang and M. Zhan, "Transient synchronous stability analysis of PMSG grid-connected system considering transient switching control under severe faults," *IEEE Trans. Power Electron.*, vol. 40, no. 5, pp. 7298–7314, May 2025.

[5] A. Nair, S. Kamalasadan, J. Geis-Schroer, S. Patel, and M. Smith, "An investigation of grid stability and a new design of adaptive phase-locked loop for wind-integrated weak power grid," *IEEE Trans. Ind. Appl.*, vol. 58, no. 5, pp. 5871–5884, Sep./Oct. 2022.

[6] E. A. Virtanen et al., "Balancing profitability of energy production societal impacts and biodiversity in offshore wind farm design," *Renew. Sustain. Energy Rev.*, vol. 158, Apr. 2022, Art. no. 112087.

[7] A. Rehman, M. A. Koondhar, Z. Ali, M. Jamali, and R. A. El-Sehiemy, "Critical issues of optimal reactive power compensation based on an HVAC transmission system for an offshore wind farm," *Sustainability*, vol. 15, no. 19, Sep. 2023, Art. no. 14175.

[8] L. Yang, Y. Chen, and X. Ma, "A State-age-dependent opportunistic intelligent maintenance framework for wind turbines under dynamic wind conditions," *IEEE Trans. Ind. Inform.*, vol. 19, no. 10, pp. 10434–10443, Oct. 2023.

[9] J. Hang, J. Zhang, M. Cheng, and J. Huang, "Online interturn fault diagnosis of permanent magnet synchronous machine using zero-sequence components," *IEEE Trans. Power Electron.*, vol. 30, no. 12, pp. 6731–6741, Dec. 2015.

[10] X. Liu, W. Miao, Q. Xu, L. Cao, C. Liu, and P. W. T. Pong, "Inter-turn short-circuit fault detection approach for permanent magnet synchronous machines through stray magnetic field sensing," *IEEE Sensors J.*, vol. 19, no. 18, pp. 7884–7895, Sep. 2019.

[11] Y. Qi, E. Bostanci, V. Gurusamy, and B. Akin, "A comprehensive analysis of short-circuit current behavior in PMSM interturn short-circuit faults," *IEEE Trans. Power Electron.*, vol. 33, no. 12, pp. 10784–10793, Dec. 2018.

[12] J. Hang et al., "A voltage-distortion-based method for robust detection and location of interturn fault in permanent magnet synchronous machine," *IEEE Trans. Power Electron.*, vol. 37, no. 9, pp. 11174–11186, Sep. 2022.

[13] Y. Zhu, S. Cai, and B. Li, "Detection and discrimination of interturn fault and high-resistance connection fault in PMSM based on deviation angle of zero sequence voltage," *IEEE Trans. Transport. Electrific.*, vol. 10, no. 3, pp. 7623–7632, Sep. 2024.

[14] Z. Xu, J. Zhang, J. Xiong, Y. Wu, and M. Cheng, "An improved high-frequency voltage injection method for interturn short-circuit fault detection in PMSMs," *IEEE Trans. Transport. Electrific.*, vol. 9, no. 2, pp. 3228–3239, Jun. 2023.

[15] R. Li, H. Fang, D. Li, R. Qu, S. Yang, and R. Wang, "A search coil design method of PMSM for detection of inter-turn short-circuit fault," *IEEE Trans. Ind. Electron.*, vol. 71, no. 4, pp. 3964–3974, Apr. 2024.

[16] D. Niu and D. Song, "Model-based robust fault diagnosis of incipient ITSC for PMSM in elevator traction system," *IEEE Trans. Instrum. Meas.*, vol. 72, 2023, Art. no. 3533512.

[17] F. Niu et al., "Accurate interturn short-circuit faults diagnosis in PMSMs under variable operating conditions by signal compensation," *IEEE Trans. Power Electron.*, vol. 40, no. 2, pp. 3530–3542, Feb. 2025.

[18] F. Niu et al., "Robust inter-turn short-circuit fault detection in PMSGS with respect to the bandwidths of current and voltage controllers," *IEEE Trans. Power Electron.*, vol. 38, no. 8, pp. 10269–10279, Aug. 2023.

[19] Y. Qin, G. -J. Li, C. Jia, and P. McKeever, "Investigation of inter-turn short-circuit fault of PM machines using PWM voltage-based modeling," *IEEE Trans. Transport. Electrific.*, vol. 10, no. 1, pp. 1324–1334, Mar. 2024.

[20] J. Hang, X. Wang, W. Li, and S. Ding, "Interturn Short-circuit fault diagnosis and fault-tolerant control of DTP-PMSM based on subspace current residuals," *IEEE Trans. Power Electron.*, vol. 40, no. 2, pp. 3395–3404, Feb. 2025.

[21] X. Fang, J. Gao, J. Lu, J. Zhang, and H. Li, "Early fault detection of stator interturn short circuit of asynchronous motor based on rotating high frequency voltage injection," *IEEE Trans. Transport. Electrific.*, vol. 11, no. 1, pp. 3377–3388, Feb. 2025.

[22] Y. He et al., "Comprehensive analysis on rotor vibration characteristics based on a novel dynamic stator interturn short circuit model of synchronous generator," *IEEE Trans. Energy Convers.*, vol. 39, no. 3, pp. 1658–1672, Sep. 2024.

[23] J. A. Rosero, L. Romeral, J. A. Ortega, and E. Rosero, "Short-circuit detection by means of empirical mode decomposition and Wigner–Ville distribution for PMSM running under dynamic condition," *IEEE Trans. Ind. Electron.*, vol. 56, no. 11, pp. 4534–4547, Nov. 2009.

[24] Y. Yu, S. Yang, X. Zhang, Y. Qu, and G. Qin, "Interturn short-circuit fault diagnosis and localization of PMSM based on current trajectory," *IEEE Sensors J.*, vol. 25, no. 1, pp. 1155–1163, Jan. 2025.

[25] H. Chen et al., "Diagnosis of interturn short-circuit of SRM based on ratio of current components," *IEEE Trans. Transport. Electrific.*, vol. 9, no. 2, pp. 3319–3327, Jun. 2023.

[26] D. Wei, K. Liu, J. Wang, S. Zhou, and K. Li, "ResNet-18-based interturn short-circuit fault diagnosis of PMSMs with consideration of speed and current loop bandwidths," *IEEE Trans. Transport. Electrific.*, vol. 10, no. 3, pp. 5805–5818, Sep. 2024.

[27] Y. Li et al., "A fault diagnosis method based on an improved deep Q-network for the interturn short circuits of a permanent magnet synchronous motor," *IEEE Trans. Transport. Electrific.*, vol. 10, no. 2, pp. 3870–3887, Jun. 2024.

[28] X. Wu, M. Li, Y. Geng, and H. Qian, "Unsupervised diagnosis of interturn short circuit of permanent magnet synchronous motor guided by density-based clustering and deep learning," *IEEE Trans. Instrum. Meas.*, vol. 74, 2025, Art. no. 350381.

[29] Z. Chen, D. Liang, S. Jia, L. Yang, and S. Yang, "Incipient interturn short-circuit fault diagnosis of permanent magnet synchronous motors based on the data-driven digital twin model," *IEEE J. Emerg. Sel. Topics Power Electron.*, vol. 11, no. 3, pp. 3514–3524, Jun. 2023.

[30] H. Cao, X. Zhang, M. Wang, K. Huo, H. Wang, and X. Feng, "Online stator interturn fault detection using Hilbert transform and neural network for traction motors of urban rail vehicles," *IEEE J. Emerg. Sel. Topics Power Electron.*, vol. 12, no. 4, pp. 4236–4248, Aug. 2024.

[31] Z. Chen, D. Liang, S. Jia, and S. Yang, "Model-based data normalization for data-driven PMSM fault diagnosis," *IEEE Trans. Power Electron.*, vol. 39, no. 9, pp. 11596–11612, Sep. 2024.

[32] R. Hu, J. Wang, A. R. Mills, E. Chong, and Z. Sun, "Current-residual-based stator interturn fault detection in permanent magnet machines," *IEEE Trans. Ind. Electron.*, vol. 68, no. 1, pp. 59–69, Jan. 2021.

[33] Z. Yu, Y. Lu, Q. An, C. Chen, Y. Li, and Y. Wang, "Real-time multiple gesture recognition: Application of a lightweight individualized 1D CNN model to an edge computing system," *IEEE Trans. Neural Syst. Rehabil. Eng.*, vol. 30, pp. 990–998, 2022.

[34] R. Pascual, K. Mahtani, E. Rivero, and C. A. Platero, "Brushless synchronous machine field winding interturn fault severity estimation through deep neural networks," *IEEE Trans. Energy Convers.*, vol. 39, no. 2, pp. 1341–1351, Jun. 2024.

Bin Sun received the B.Sc. degree in electrical engineering and automation from Nantong University, Nantong, China, in 2023. He is currently working toward the M.Sc. degree in electrical engineering with Hohai University, Nanjing, China.

His current research interest includes fault diagnosis of permanent magnet direct-driven wind power systems.

Ying Zhu (Member, IEEE) received the B.Sc. and Ph.D. degrees in electrical engineering from Southeast University, Nanjing, China, in 2008 and 2014, respectively.

Since 2014, she has been with Hohai University, Nanjing, China, where she is an Associate Professor with the School of Electrical and Power Engineering. In recent years, she has authored or coauthored more than 30 technical articles. Her research interests include the areas of control and applications of wind power generation systems and novel permanent magnet machine control.

Zhinong Wei (Member, IEEE) received the B.S. degree from Hefei University of Technology, Hefei, China, the M.S. degree from Southeast University, Nanjing, China, and the Ph.D. degree from Hohai University, Nanjing, China, in 1984, 1987, and 2004, respectively, all in power system automation.

He is currently a Professor of electrical engineering with the School of Electrical and Power Engineering, Hohai University, Nanjing, China. His research interests include integrated energy systems, power system state estimation, smart distribution systems, and integration of distributed generation into electric power systems.